

Combined Charge and Spin Density Experimental Study of the Yttrium(III) Semiquinonato Complex $\text{Y}(\text{HBPz}_3)_2(\text{DTBSQ})$ and DFT Calculations

N. Claiser,[†] M. Souhassou,[†] C. Lecomte,[†] B. Gillon,^{*,‡} C. Carbonera,[§] A. Caneschi,[§] A. Dei,[§] D. Gatteschi,[§] A. Bencini,[§] Y. Pontillon,^{¶,+} and E. Lelièvre-Berna[#]

Laboratoire de Cristallographie et Modélisation des Matériaux Minéraux et Biologiques, UMR CNRS 7036, Université Henri Poincaré-Nancy I, BP 239, F-54506 Vandœuvre-les-Nancy Cedex, France, Laboratoire Léon Brillouin, (CEA-CNRS), C.E. Saclay, F-91191 Gif-sur-Yvette, France, Dipartimento di Chimica e Udr INSTM di Firenze, Via della Lastruccia 3, I-50019 Sesto Fiorentino, Italy, DRN/DEC, CENG, 17 Avenue des Martyrs, F-38041 Grenoble Cedex 9, France, and Institut Laue-Langevin, 6 Rue Jules Horowitz, BP156, F-38042 Grenoble Cedex 9, France

Received: July 20, 2004; In Final Form: November 18, 2004

High-resolution X-ray diffraction and polarized neutron diffraction experiments have been performed on the Y-semiquinonato complex, $\text{Y}(\text{HBPz}_3)_2(\text{DTBSQ})$, in order to determine the charge and spin densities in the paramagnetic ground state, $S = 1/2$. The aim of these combined studies is to bring new insights to the antiferromagnetic coupling mechanism between the semiquinonato radical and the rare earth ion in the isomorphous $\text{Gd}(\text{HBPz}_3)_2(\text{DTBSQ})$ complex. The experimental charge density at 106 K yields detailed information about the bonding between the Y^{3+} ion and the semiquinonato ligand; the topological charge of the yttrium atom indicates a transfer of about 1.5 electrons from the radical toward the Y^{3+} ion in the complex, in agreement with DFT calculations. The electron density deformation map reveals well-resolved oxygen lone pairs with one lobe polarized toward the yttrium atom. The determination of the induced spin density at 1.9 K under an applied magnetic field of 9.5 T permits the visualization of the delocalized magnetic orbital of the radical throughout the entire molecule. The spin is mainly distributed on the oxygen atoms [O_1 (0.12(1) μ_B), O_2 (0.11(1) μ_B)] and the carbon atoms [C_{21} (0.24(1) μ_B), C_{22} (0.20(1) μ_B), C_{24} (0.16(1) μ_B), C_{25} (0.12(1) μ_B)] of the carbonyl ring. A significant spin delocalization on the yttrium site of 0.08(2) μ_B is observed, proving that a direct overlap with the radical magnetic orbital can occur at the rare earth site and lead to antiferromagnetic coupling. The DFT calculations are in good quantitative agreement with the experimental charge density results, but they underestimate the spin delocalization of the oxygen toward the yttrium and the carbon atoms of the carbonyl ring.

Introduction

The mechanism of exchange interactions between rare earth ions and organic radicals is far from being understood.¹ The difficulty is associated with the largely unquenched orbital moment present in most rare earth ions, the notable exception being the $S = 7/2$ ion, gadolinium(III). Consequently, complexes of this ion have been the most thoroughly investigated, taking advantage of the spin-only nature of the magnetic moment, which minimizes the complications associated with magnetic anisotropy.

In contrast to the complexes formed by a Gd^{3+} ion and a nitronyl nitroxide radical (NIT),² which usually present ferromagnetic intramolecular coupling, the $\text{Gd}(\text{HBPz}_3)_2(\text{DTBSQ})$ complex, where DTBSQ = di-*tert*-butylsemiquinonato and HBPz_3 = hydrotrispyrazolylborate, is characterized by antiferromagnetic coupling between the rare earth ion and the

semiquinonato radical, corresponding to an $S = 3$ ground spin state.³ The nature of the magnetic interaction between the rare earth ion Gd^{3+} and a radical was interpreted as resulting from the sum of two contributions:⁴ one from the direct overlap of the radical π orbital with the 4f orbitals, resulting in antiferromagnetic coupling, and the other due to the 4f orbitals' polarization by the spin delocalized from the radical toward the unoccupied 5d or 6s Gd^{3+} orbitals,⁵ leading to ferromagnetic coupling. This mechanism has recently been tested through XMCD measurements.⁶

To acquire independent information on these mechanisms, we decided to investigate the isomorphous complex, $\text{Y}(\text{HBPz}_3)_2(\text{DTBSQ})$, where the nonmagnetic Y^{3+} ion replaces Gd^{3+} , which can provide information on the role of closed shells and empty orbitals. To obtain as much experimental information as possible, we used a combined approach, which involves measuring the charge density through high-resolution X-ray diffraction experiments at 106 K and determining the spin density through polarized neutron diffraction experiments at 1.9 K. Only a few of such investigations involving both charge and spin densities have been performed until now on molecule-based magnetic compounds.^{7–12} The charge density determination allows investigations into the nature of the bonding between Y and the semiquinonato ligand. Meanwhile, the spin distribution gives access to the delocalization of the radical magnetic orbital

* Author to whom correspondence should be addressed. E-mail: gillon@llb.saclay.cea.fr.

[†] Université Henri Poincaré-Nancy I.

[‡] CEA-CNRS.

[§] Dipartimento di Chimica e Udr INSTM di Firenze.

[¶] CENG.

⁺ Present address: DEN/DEC, CEN Cadarache, 13108 Saint Paul Lez Durance, France.

[#] Institut Laue-Langevin.

TABLE 1: Experimental and Data Collection Details (X-ray and Neutrons)

chemical formula	Crystallographic data		YO ₂ N ₁₂ C ₃₂ B ₂ H ₄₀
space group, cell setting			P2 ₁ /c, monoclinic
X-ray Data Collection (Nonius Kappa CCD)			
T (K), wavelength (Å)	106, 0.71074 Mo Kα		
a, b, c (Å); β (deg)	12.5943(1), 14.8920(1), 19.5690(1); 98.428(1)		
Z, calculated D _x (g/cm ³)	4, 1.344		
scan method, oscillation width (deg)	φ and ω rotations, 2.0		
exposure time per degree (s)	150 and 300		
crystal to detector distance (mm)	40		
No. of frames, No. of measured reflns	1371, 385562		
range of h,k,l, (sinθ/λ) _{max} (Å ⁻¹)	-27 < h < 26, 0 < k < 30, 0 < l < 41, 1.08		
μ _{RX} (mm ⁻¹), A _{min} , A _{max}	1.6583, 0.698 and 0.805		
No. of independent reflns (I>0)	36109		
R _{int} ^a (all data) (%), overall completeness (%)	7.75, 91.0		
Neutron Data Collection (ILL, D9, Grenoble) and Refinement Conditions			
T (K), wavelength (Å)	10, 0.8398		
a, b, c (Å); β (deg)	12.567(1), 14.832(1), 19.619(2); 98.150(1)		
No. of params and independent reflns	358, 1997		
No. of significant reflns: F ₀ >4 σ(F ₀)	1643		
range of h,k,l, (sinθ/λ) _{max} (Å ⁻¹)	-12 < h < 2, -12 < k < 2, -15 < l < 15, 0.91		
μ _N (cm ⁻¹) (λ = 1 Å)	1.69		
R _{int} ^b (%), R _σ ^c (%)	3.80, 6.92		
Polarized Neutron Data Collection (ILL, D3, Grenoble)			
T (K), H (tesla), wavelength (Å)	1.9, 9.5, 0.852		
beam polarization, flipping efficiency	0.955(4), 1.000(1)		
vertical axis	2, -2, 1		
No. of independent reflns	157		
No. of significant reflns F _M > σ(F _M)	95		

$$^a R_{\text{inf}} = \frac{\sum_{\vec{h}} \sqrt{\frac{N}{N-1}} \sum_{i=1}^{N_{\text{equivalent}}} |I_i - \langle I \rangle|}{\sum_{\vec{h}} \sum_i |I_i|} \quad ^b R_{\text{int}} = \frac{\sum_{\vec{h}} |F_{\text{obs}}^2 - \langle F_{\text{obs}}^2 \rangle|}{\sum_{\vec{h}} F_{\text{obs}}^2} \quad ^c R_{\sigma} = \frac{\sum_{\vec{h}} \sigma(F_{\text{obs}}^2)}{\sum_{\vec{h}} F_{\text{obs}}^2}$$

throughout the molecule, especially on the metal site,¹³ and it permits a direct verification of the validity of the proposed mechanism. State-of-the-art DFT calculations have finally allowed a quantitative description of the bonding between rare earth ions and semiquinonate ligands.

Experimental Section and Calculation Method

Synthesis. The potassium salt of the ligand, KHBpz₃, was obtained following the standard procedure previously described.¹⁴ The metathetic reaction between the parent yttrium–benzoate derivative and 3,5-di-*tert*-butylcatechol was performed using an analogous procedure performed for rare earth derivatives.¹⁵ The precipitate³ was collected and dissolved in a 1:20 mixture of CHCl₃/hexane and stored for about 2 weeks at −5 °C. Well-shaped dark-blue crystals were collected, and five of them were placed in a beaker together with a new solution of the complex obtained by dissolving the starting powdered product with hexane only. The beaker was sealed and stored at −30 °C for 2 weeks. The operation was repeated a number of times in order to obtain a 6 mm³ single crystal of the nonsolvate form of the Y(HBPz₃)₂(DTBSQ) complex.

X-ray Data Collection. A black-blue single crystal of dimensions 0.22 × 0.29 × 0.22 mm³ was mounted on a Nonius Kappa-CCD diffractometer using graphite monochromatized Mo Kα radiation. The crystal was cooled to 106 K using a N₂ Oxford cryosystem cooling device. A total of 1371 images up to a resolution of 1.08 Å^{−1}, sin(θ)/λ, have been collected. Detector-to-crystal distance was kept fixed, while two different exposure times per degree were used: 150 s deg^{−1} for low-

resolution sets and 300 s deg^{−1} for high-resolution data. The final cell parameters were obtained at the end of the overall data collection by refinement against the 385 562 collected reflections. More details about the experimental settings and crystal data are reported in Table 1.

Reflections were indexed and integrated using the DENZO¹⁶ program implemented in the HKL2000 package.¹⁶ Then, the data were corrected from Lorentz polarization and absorption effects (ABSORB¹⁷). The data were sorted, scaled, and averaged using SORTAV.¹⁸ The crystal did not present any decay during the data collection, as indicated by the evolution of the interframe scale factors versus time. The 385 562 observed reflections were merged into 36 109 independent ones. This data collection strategy enabled a high redundancy (10.7 on average), improving the precision of the intensities that is required for an accurate crystallographic study. The internal agreement index for the whole data set was *R*₁ = 7.75% without any σ cutoff (Table 1); this rather high value is due mainly to the lower signal-over-noise ratio of the high-resolution data (see Supporting Information). The reflections with negative intensities were re-estimated using a Bayesian approach (BAYES program).¹⁹

Neutron Diffraction Data Collection at 10 K. A four-circle neutron experiment was performed in order to determine the low-temperature nuclear structure factors necessary to analyze the polarized neutron data. A crystal of Y(HBPz₃)₂(DTBSQ) of 6 mm³ size was set in the diffractometer on the D9 diffractometer of the ILL (Institut Laue Langevin, Grenoble, France) and cooled to 10 K (see Table 1).

After data reduction, the integrated intensities of 1997 unique reflections were obtained, allowing the determination of the experimental values of the square of the nuclear structure factors $|F_N(hkl)|^2$ after the Lorentz correction (COLL5 program²⁰). No absorption corrections were applied because of the small value of the linear absorption coefficient, estimated to be 1.69 cm^{-1} .

Polarized Neutron Diffraction Experiment. The polarized neutron diffraction technique was used to determine the spin density distribution in the $\text{Y}(\text{HBPz}_3)_2(\text{DTBSQ})$ radical.²¹ The sample is a paramagnetic single crystal in which a magnetization is induced by a large vertical magnetic field. This technique consists of measuring the ratio between the diffracted intensities, for a set of Bragg reflections, when the incident neutron beam polarization is alternately parallel or antiparallel to the vertical direction. The so-called flipping ratio, $R(\vec{K})$, is related to the magnetic $F_M(\vec{K})$ and nuclear $F_N(\vec{K})$ structure factors of the reflection with scattering vector \vec{K} :

$$R(\vec{K}) = \frac{F_N^2 + 2q^2 F_N F_M + q^2 F_M^2}{F_N^2 - 2q^2 F_N F_M + q^2 F_M^2} \quad (1)$$

where q is equal to $\sin \alpha$, with α being the angle between the scattering vector \vec{K} and the direction of the induced magnetic moments in the sample.

The magnetic structure factors, $F_M(\vec{K})$, are the Fourier components of the magnetization density. In the case of an organic radical, there is no orbital contribution to the induced magnetization density which is then identical to the induced spin density, $\rho_s(\vec{r})$. The experimental value of $F_M(\vec{K})$ is deduced from eq 1, knowing the experimental flipping ratio and the nuclear structure factor. The spin density is retrieved from the experimental set of $F_M(\vec{K})$ either by Fourier summation or with help of the Maximum of Entropy method²² or by a model refinement.²³

The magnetic behavior of $\text{Y}(\text{HBPz}_3)_2(\text{DTBSQ})$ is in agreement with what is expected for a well-isolated $S = 1/2$ system. The magnetization at 1.8 K reaches the saturation value expected for a $S = 1/2$ with $g = 2.00$ spin state. The χT versus T curve (given in the Supporting Information) shows a Curie–Weiss behavior with a constant value of $0.38 \text{ emu} \cdot \text{K} \cdot \text{mol}^{-1}$ corresponding to a $S = 1/2$ system with $g = 2.01$ down to about 20 K, where a small decrease in the χT value indicates the presence of some intermolecular antiferromagnetic interaction. A crystal of $\text{Y}(\text{HBPz}_3)_2(\text{DTBSQ})$ of 6 mm^3 size (different from the one used for D9) was set in the cryomagnet on the D3 diffractometer at the ILL (Institut Laue Langevin, Grenoble, France), with the $[2, -2, 1]$ direction vertical, and cooled to 1.9 K under an applied field of 9.5 T (see Table 1). Under these conditions, magnetic saturation is achieved. The wavelength was 0.852 \AA . Only reflections with a sufficiently large nuclear structure factor ($|F_N| > 5 \times 10^{-12} \text{ cm}$) were measured in order to avoid problems with multiple reflections. A set of 198 hkl reflections was collected with $h_{\text{max}} = 6$, $k_{\text{max}} = 7$, and $l_{\text{max}} = 8$ leading to 157 unique reflections. The low-temperature nuclear structure obtained from the D9 data collection was used to derive the experimental magnetic structure factors from the flipping ratios. A correction for the nuclear polarization of the hydrogen nuclei was applied.

Density Functional Theory Computational Details. SCF Density Functional calculations were performed with the Amsterdam Density Functional (ADF) program package (version 2000.03),²⁴ using both the Local Density Approximation (LDA), with the Slater exchange²⁵ potential and the correlation potential (functional V) of Vosko–Wilk–Nusair (VWN),²⁶ and

the Generalized Gradient Approximation (GGA) in the form suggested by Perdew and Wang (PW91).²⁷ All the calculations were spin unrestricted and performed using the atomic coordinates obtained from the experimental neutron diffraction structure of $\text{Y}(\text{HBPz}_3)_2(\text{DTBSQ})$ at 10 K, except for the *tert*-butyl groups which were replaced with methyl groups (C–H bond distance of 0.95 \AA). Relativistic effects were taken into account using the Zeroth Order Regular Approximation (ZO-RA).²⁸ Spin–orbit coupling was not included. The Slater-Type Orbitals basis set that comes with the ADF package has been used throughout. Triple- ζ bases were used for Y with the core frozen up to 4p. Double- ζ bases were applied to the other atoms; the basis sets for C, O, and N were extended, including a p-polarization function. The 1s orbital of the non-hydrogen atoms has been kept frozen in all of the calculations. The overall symmetry was C_1 in any case. With these settings, the number of basis functions was 722, and the total number of atoms in the molecule is 71.

Charge and Spin Density Modelization. X-ray and Neutron Structure Refinement. The structure of the title compound has been previously described at room temperature (X-ray data).²⁹ The room-temperature atom's positions were used as the starting x , y , and z parameters for the X-ray and neutron refinements. In the X-ray case, all hydrogen atoms were located in difference Fourier maps after refinement of anisotropic thermal displacement parameters (ADPs) of non-hydrogen atoms (SHELX,^{30,31} Independent Atom Model, IAM). For neutron data, due to the relatively small number of measured structure factors, only positions and isotropic thermal parameters were refined with SHELX. The extinction was refined but was found to be negligible. The refinement statistical indices are reported in Table 2.

Multipolar Model for Charge and Spin Density Determination. The Hansen & Coppens formalism²⁹ was used to model both electron and spin density distributions:

$$\rho(\vec{r}) = \rho_{\text{core}}(r) + P_v \kappa^3 \rho_v(\kappa r) + \sum_{l=0}^{l_{\text{max}}} \kappa'^3 R_{n_l}(\kappa' r) \sum_{m=-l}^{+l} P_{lm} y_{lm}(\theta, \varphi) \quad (2)$$

with

$$R_{n_l}(r) = \frac{\xi_1^{n_l+3}}{(n_l + 2)!} r^{n_l} e^{-\xi_1 r} \quad (3)$$

The first two terms, $\rho_{\text{core}}(r)$ and $\rho_v(r)$, are the spherically averaged core and the valence electron densities of the free atom, respectively. In the case of charge density, the terms are calculated from Roetti and Clementi wave functions,³³ and in the case of spin density, they are described by spherical densities with a Slater-type radial function, as that used for the multipolar development. The last term is a projection of the valence (or spin) deformation density on spherical harmonic functions in real form, y_{lm} . P_v is the valence (or spin) electron populations, and κ and κ' are contraction expansion parameters. The radial functions, $R_{n_l}(r)$, were chosen as Slater-type (eq 3).

Charge Density Refinements. For the charge density refinement, the n_l values are 2–2–3 ($l_{\text{max}} = 3$), except for yttrium for which $n_l = 6-7-8-8$ ($l_{\text{max}} = 4$) and for hydrogen atoms ($l_{\text{max}} = 1$; $n_l = 0-1$). The ξ_1 parameters are 6.00, 3.80, 3.00, and 2.50 Bohr^{-1} (single- ζ) for Y, O, C, and B atoms, respectively. Two different ξ_1 parameters were assigned to the nitrogen atoms, 3.00 Bohr^{-1} for N linked to boron atoms and 3.40 Bohr^{-1} for N coordinating the yttrium atom. A hydrogen-

TABLE 2: Agreement Indices and Agreement Factors

(a) At Different Stages of the Structure and Charge Density Refinement: IAM, HO, and LO Stand for Independent Atoms Model, High Order, and Low Order, Respectively							
program used	sin θ/λ (\AA^{-1})	I/σ	R % ^a	R_w % ^b	GOF ^c	N_{obs}	N_{var}
SHELX (IAM)							
Structure Refinement							
neutron data	all data	2	7.65	16.0	1.153	1643	358
X-ray data	all data	2	3.74	17.27	0.676	11388	602
Charge Density Refinement							
MOPRO							
IAM	<0.9	>3	2.26	2.66	0.78	9633	602
IAM HO	>0.7	>3	3.80	7.10	1.04	2509	441
Multipolar Model	<0.9	>3	1.47	1.47	0.42	9633	1052
(b) Agreement factors at different stages of the spin density refinement for the two different radial models used							
Spin Density Refinement							
multipolar model ^d	Radial model A			Radial model B			
	R_w %	GOF	N_{var}	R_w %	GOF	N_{var}	
I	14.96	1.27	12	15.34	1.29	10	
II	14.07	1.21	14	14.12	1.21	12	
III	13.14	1.17	20	13.37	1.18	18	
IV	12.12	1.10	22	12.19	1.09	20	

$$^a R = \frac{\sum_{\vec{H}} \frac{1}{k} |F_{\text{obs}}(\vec{H})| - |F_{\text{calc}}(\vec{H})|}{\sum_{\vec{H}} \frac{1}{k} |F_{\text{obs}}(\vec{H})|} \quad ^b R_w = \sqrt{\frac{\sum_{\vec{H}} w \left[\frac{1}{k} |F_{\text{obs}}(\vec{H})| - |F_{\text{calc}}(\vec{H})| \right]^2}{\sum_{\vec{H}} \frac{1}{k^2} w |F_{\text{obs}}(\vec{H})|^2}} \quad ^c \text{GOF} = \sqrt{\frac{\sum_{\vec{H}} w \left[\frac{1}{k} |F_{\text{obs}}(\vec{H})| - |F_{\text{calc}}(\vec{H})| \right]^2}{N_{\text{obs}} - N_{\text{var}}}}, w = \sigma^{-2}(F).$$

^d I = (monopoles on O, C); II = (monopoles O, C_{Me} + 2p C_{ring}); III = (monopoles on C_{Me} + 2p C_{ring} + (2s,2p) O); IV = (III + monopoles (4s, 5d) on Y).

contracted form factor ($\kappa = 1.16$)³⁴ was used; the anomalous dispersion coefficients were those of Cromer,³⁵ and an electroneutrality constraint was applied during the refinements. Starting structural parameters were obtained from the SHELX refinement. Position and ADPs of non-H atoms were first refined against high-order (HO) X-ray reflections; then, all hydrogen atom parameters were refined against low-order (LO) reflections. To avoid biases in the electron density modeling due to the shift of the electron density distribution toward the atom linked to H, each carbon and boron–hydrogen distance was adjusted to the value obtained from our neutron diffraction experiment (average distances: C–H = 1.082(6) Å; B–H = 1.20 ± 0.03 Å). Then, the hydrogen positions were restrained according to the above values ($\sigma = 0.005$)³⁶ during the entire refinement. All chemically equivalent atoms of the HBPz₃, including boron atoms, were constrained to have the same charge density parameters. The same κ , κ' values were assigned to pseudo chemically equivalent atoms of the semiquinonate radical (for example, C₂₃ and C₂₅ in Figure 1).

The multipolar refinement was performed with MOPRO³⁶ for 9633 reflections, with $I > 3\sigma$ and $\sin \theta/\lambda < 0.9 \text{ \AA}^{-1}$. This new multipole program allows bond distance and charge density parameter restraints to be applied, which can be necessary for large molecules. The agreement indices at the end of the full multipole model are excellent ($R = 1.47\%$, $R_w = 1.47\%$, and $\text{GOF} = 0.42$), attesting for the quality of the data used for the refinement. The average estimated standard deviation of the electron density is defined by

$$\sigma_1(\rho) = \frac{\sqrt{\sum_{\vec{H}} (\Delta F(\vec{H}))^2}}{V} \quad (4)$$

where $\Delta F(\vec{H})$ is the difference between observed and calculated structure factors. The obtained $\sigma_1(\rho)$ value is $\sigma_1(\rho) = 0.03 \text{ e \AA}^{-3}$.

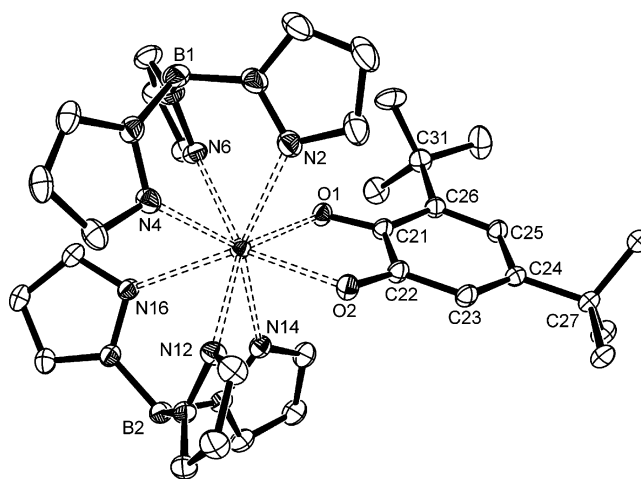


Figure 1. Molecular structure of the Y(HBPz₃)₂(DTBSQ) complex at 106 K from X-ray diffraction. Anisotropic thermal ellipsoids are drawn at 50% probability.

Table 2a summarizes the refinement indices obtained for all refinements. Atomic positions and ADPs at the end of the multipolar refinement are given as Supporting Information, as well as interatomic distances.

Two kinds of density maps are commonly used to analyze the modeled electron density. First, the residual density (eq 5), which is the difference between modeled and observed electron densities, allows judging of the refinement's quality in direct space:

$$\Delta \rho_{\text{resi}}(\vec{r}) = \frac{1}{V} \sum_{\vec{H}} \left(\frac{1}{k} |F_{\text{obs}}(\vec{H})| - |F_{\text{calc}}(\vec{H})| \right) e^{i\Phi_{\text{calc}}} e^{-2i\pi \vec{H} \cdot \vec{r}} \quad (5)$$

where F_{obs} and F_{calc} are the structure factor amplitudes observed and calculated using the multipolar atom model, respectively;

k is the scale factor, and Φ_{calc} is the best structure factor phase calculated from the multipolar model. The static deformation density map allows analyzing of the modeled electron density (eq 6), as defined by the difference between the modeled static total electron density (eq 2) and the sum of spherical averaged independent atom densities:

$$\Delta\rho(\vec{r}) = P_v\kappa^3\rho_v(\kappa r) - N_v\rho_v(r) + \sum_{l=0}^{l_{\max}} \kappa'^3 R_l(\kappa' r) \sum_{m=-l}^{+l} P_{lm} y_{lm}(\theta, \varphi) \quad (6)$$

where N_v is the number of valence electrons of the free atom. In this paper, only the map calculated and plotted in the plane of the semiquinonate ring is presented.

The total electron density can be analyzed in a more quantitative way using the “Atoms In Molecules, A Quantum Theory”.³⁷ From the spatial distribution of the electron density, one can derive the gradient trajectories ($\nabla\rho$), the laplacian distribution ($\nabla^2\rho(\vec{r})$), and the location of all critical points (CP), that is, where the gradient of ρ vanishes, and its associated topological features. The nature of the CP is determined by the eigenvalues (curvatures) of the Hessian matrix ($\partial^2\rho(r)/\partial x_i\partial x_j$). This topological analysis allows the decomposition of the total electron density on atomic basins; the volume integration carried out on these basins gives access to the net atomic charges. A new version of the NEWPROP³⁸ program was used to locate the CP and to calculate the topological properties and integrated charges of the modeled electron density. As interatomic contacts can give rise to electron transfer, the knowledge of precise atomic charges permits a better understanding of the possible interatomic interactions.

Spin Density Determination. For the spin density model refinement,²³ only the second and third terms in eq 2 are used as there is no core contribution to the spin density:

$$\rho_s(\vec{r}) = P_v\kappa^3\rho_v(\kappa r) + \sum_{l=0}^{l_{\max}} \kappa'^3 R_l(\kappa' r) \sum_{m=-l}^{+l} P_{lm} y_{lm}(\theta, \varphi) \quad (7)$$

The valence spin density is described by a monopole function with a Slater-type radial function (see eq 3). This term is used only for the Y atom in order to take into account a 5s contribution ($n = 8$), in addition to the 4d contribution ($n = 6$) described by the monopole of the deformation term. For all other atoms, only the deformation part is used, and a value of $n = 2$ is taken for all multipoles on the C and O atoms in order to apply constraints on populations corresponding to 2p-type densities. The spin populations are deduced from the refinement by taking the value of the refined monopole populations ($P_{00} + P_v$) in eq 7. In contrast, for charge density refinements, the charge is evaluated using the P_v parameters (the P_{00} values are not refined) or the topological approach. Two models have been used for the spin densities that differ by the radial expansion coefficients. In model A, the radial exponents were taken from the literature³⁹ and refined for the C and O atoms; in model B, the radial parameters are those of the valence electron density from the charge density refinement (with the difference that Slater-type functions were used instead of form factors: for Y, $n = 8$, $\zeta = 2.6$ for 5s-type density and $n = 6$, $\zeta = 3.9$ for 4d-type density; for O, $n = 2$, $\zeta = 4.3$; and for C, $n = 2$, $\zeta = 3.1$ for all multipoles).

In both models, the final spin density is described as a sum of (i) densities corresponding to a linear combination of 2s and 2p orbitals on the coordinating oxygen atoms allowing some

TABLE 3: Selected Interatomic Distances (in Å) at 106 and 10 K

	X-rays ($T = 106$ K)	neutrons ($T = 10$ K)
Y–O ₁	2.2951(6)	2.29(1)
Y–O ₂	2.3135(9)	2.33(1)
Y–N ₂	2.5245(10)	2.51(1)
Y–N ₄	2.4959(11)	2.49(1)
Y–N ₆	2.4609(8)	2.47(1)
Y–N ₁₂	2.4623(9)	2.46(1)
Y–N ₁₄	2.5410(9)	2.58(1)
Y–N ₁₆	2.5212(10)	2.52(1)
O ₁ –C ₂₁	1.281(1)	1.30(1)
O ₂ –C ₂₂	1.284(1)	1.26(1)
C ₂₁ –C ₂₂	1.469(1)	1.49(1)
C ₂₁ –C ₂₆	1.439(1)	1.42(1)
C ₂₂ –C ₂₃	1.422(1)	1.43(1)
C ₂₃ –C ₂₄	1.372(1)	1.36(1)
C ₂₄ –C ₂₅	1.437(1)	1.46(1)
C ₂₄ –C ₂₇	1.524(1)	1.54(1)
C ₂₅ –C ₂₆	1.376(1)	1.38(1)
C ₂₆ –C ₃₁	1.528(1)	1.52(1)

hybridization, (ii) 2p-type densities on the carbonyl carbon atoms, with the constraint that the direction of 2p atomic orbitals is the same for all carbon atoms,^{40,41} (iii) spherical densities on the carbon atoms of the two methyl groups, and (iv) spherical density on Y, equal to the sum of 4d and 5s contributions.

No attempts for spin density refinements on other atoms were tried due to the small number of reflections. The two different models of the spin density were refined against 95 experimental magnetic structure factors with $F_M > \sigma(F_M)$.

Table 2b summarizes the agreement factors obtained at different stages of the refinements. First, a spherical refinement on the O and C atoms of the semiquinonate group was performed. Second, a refinement of the shape of the carbon densities of the carbonyl ring due to 2p orbitals was introduced. The quality of the refinement was then improved by refining the shape of the oxygen densities allowing for some hybridization. Finally, the refinement of an additional spherical density on the yttrium atom, including 4d- and 5s-type contributions, clearly improves the agreement factors.

Results and Discussion

Crystal Structure. The X-ray molecular structure of Y(HBPz₃)₂(DTBSQ) at 106 K as derived from the multipolar refinement is represented in Figure 1. The intramolecular distances for the Y coordination sphere and the semiquinonate radical, at 106 and 10 K, are given in Table 3. At 10 K, both Y–O₁ and Y–O₂ distances do not change (2.29(1) and 2.33(1) Å, respectively, versus 2.295(1) and 2.313(1) Å at 106 K). At low temperature, the Y–N bonds involving N₄, N₆, and N₁₂ remain shorter than those involving N₂, N₁₄, and N₁₆ (2.47(2) and 2.54(1) Å, respectively, at 10 K). The corresponding distances at 106 K are 2.43(2) and 2.53(1) Å.

The average bond lengths observed at 106 K in the semiquinonate radical are close to those given in the literature.^{42–47} As previously described in semiquinonate radicals^{29,42,43}, a peculiar bond length distribution arises, consisting of four long bonds, C₂₁–C₂₂, C₂₁–C₂₆, C₂₂–C₂₃, and C₂₄–C₂₅ (1.422(1)–1.469(1) Å), and two short ones, C₂₃–C₂₄ and C₂₅–C₂₆ (1.372(1) and 1.376(2) Å, respectively). This C–C distribution remains the same at 10 K. The two C–O bonds present similar distances at 106 K (C₂₁–O₁, $d = 1.281(1)$ Å; C₂₂–O₂, $d = 1.284(1)$ Å), but when temperature decreases to 10 K, C₂₂–O₂ ($d = 1.26(1)$ Å) is marginally shorter than C₂₁–O₁ ($d = 1.30(1)$ Å), which

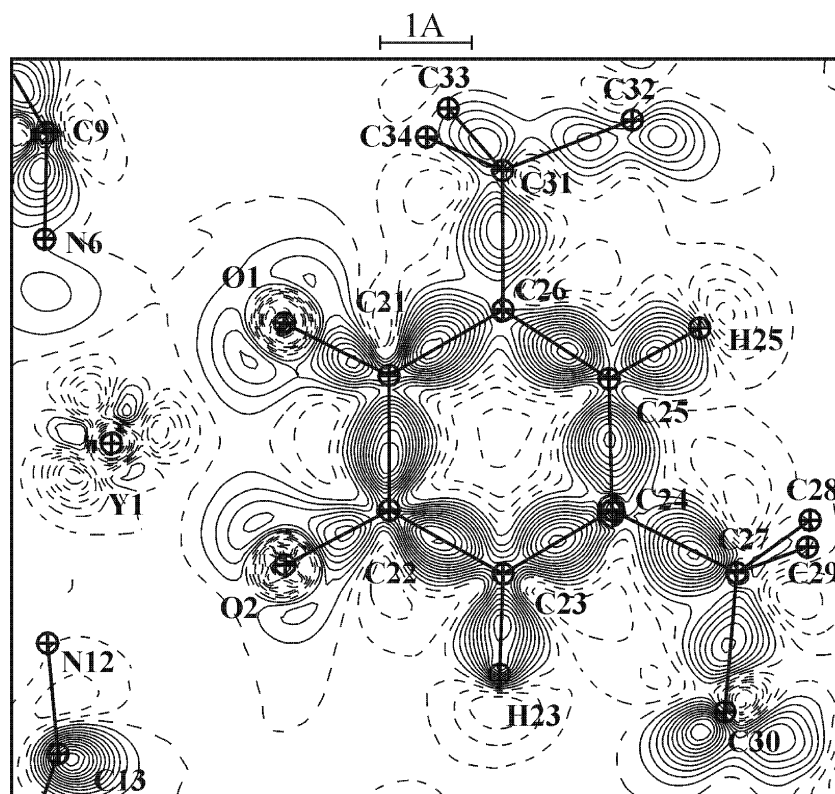


Figure 2. Experimental static deformation density map in the semiquinonate ring. Contours of $0.05 \text{ e } \text{\AA}^{-3}$: positive (continue), negative (dashed), and zero (long dashed).

TABLE 4: Experimental Net Atomic Charges and Volumes at 106 K Obtained by Integration over the Topological Atomic Basins (C_{NB} and C_N Are Carbon Atoms Linked to N–B and to N–Y Bonds, Respectively)

atom	$Q_{\text{int}} (\text{e})$	volume (\AA^3)	atom	$Q_{\text{int}} (\text{e})$	volume (\AA^3)
Y	1.53	13.1	C ₂₁	0.57	7.82
O ₁	−1.08	15.2	C ₂₂	0.44	8.89
O ₂	−0.99	20.1	C ₂₃	0.01	16.4
N ₂	−0.58	14.9	C ₂₄	0.29	8.77
N ₄	−0.56	13.7	C ₂₅	−0.25	15.1
N ₆	−0.53	11.3	C ₂₆	0.42	9.03
N ₁₂	−0.51	11.2	C ₂₇	0.19	6.09
N ₁₄	−0.59	12.1	C ₃₁	0.21	6.04
N ₁₆	−0.57	11.7			
N ₁	−0.95	13.7	$\langle C_{NB} \rangle$	0.32	12.0
N ₃	−0.87	12.4	$\langle C \rangle$	−0.24	15.9
N ₅	−0.96	14.4	$\langle C_N \rangle$	0.18	13.6
N ₁₁	−0.94	12.1			
N ₁₃	−0.87	12.1	B ₁	2.54	0.82
N ₁₅	−0.96	12.2	B ₂	2.53	0.83

could indicate a slight dissymmetry between the two oxygen atoms.

Experimental Electron Density. The residual density does not exceed $0.10 \text{ e } \text{\AA}^{-3}$ on the organic parts of the molecule, indicating the good quality of the density model. However, close to the yttrium atom, the residual density still reaches $0.25 \text{ e } \text{\AA}^{-3}$. Besides the accumulation of errors close to heavy atoms and despite careful absorption corrections, this reveals the difficulties in modeling heavy atom electron density.⁴⁸

The static deformation electron density map as obtained at the end of the multipole refinement is given in Figure 2. Table 4 presents the topological charges obtained by integration over the atomic basins of the yttrium complex. Formally, the central ion carries a +3 charge, with each surrounding ligand (the semiquinonate radical and the two HBPz₃) carrying a −1 charge. The experimental topological charges are −1.13 and −1.07 on

both HBPz₃, +1.53 on yttrium, and +0.91 e on the semiquinonate radical. This observation indicates an electron transfer of approximately 1.5 e from the semiquinonate radical to the central ion.

In the pyrazolyl parts, the two nitrogen atom-types possess an identical topological volume ($\langle V \rangle = 12.8$ and 12.5 \AA^3); they, however, carry different negative charges ($\langle Q \rangle = -0.93(4)$ and $-0.56(3) \text{ e}$), the largest charge being carried by the nitrogen linked to the boron atom. This is in line with the strong electropositive nature of the boron atom which entails a significant positive charge and a very small volume ($\langle Q \rangle = +2.54(1) \text{ e}$, $\langle V \rangle = 0.83(1) \text{ \AA}^3$). The carbon atoms present a charge alternation (+0.32(2), −0.24(2), and +0.18(2) on average), with the more highly charged positive carbon being bonded to the more negatively charged nitrogen.

The semiquinone radical is highly polarized; each oxygen atom carries a large negative charge ($Q = -1.08$ and -0.99 e for O₁ and O₂, respectively), mainly counterbalanced by the positive charge of the *tert*-butyl fragments. It is interesting to stress that surprisingly the volume occupied by the less-charged O₂ atom (20.1 \AA^3) is significantly greater than that of O₁ (15.2 \AA^3). Moreover, the highly charged C₂₁ (+0.57 e) is concentrated in a small volume ($V = 7.8$ versus 8.9 \AA^3 for C₂₂, $Q = +0.44 \text{ e}$), confirming the dissymmetry between the two C–O groups. These volume differences are induced by the asymmetry of the semiquinonate radical due to the methyl group positions.

Another interesting point is the shape of the deformation density around the two oxygen atoms (Figure 2). The lone pair densities of the two oxygen atoms are well resolved, with one lobe polarized toward the yttrium atom. In fact, these two atoms present not only two localized peaks but also an increase of deformation density located approximately 0.55 \AA from the oxygen nucleus directed toward Y. It surrounds a hole of negative deformation density on the atomic position. This density shape is similar to that observed in the oxygen atoms

TABLE 5: Experimental Spin Populations for Y(HBPz₃)₂(DTBSQ) from the Final Multipole Refinements for the Radial Model A and Model B

	Model A	Model B
Radial Coefficients ζ value (au ⁻¹)		
ζ_Y 5s	2.50	3.353
ζ_Y 4d	7.98	5.030
ζ_O	3.1(7)	4.132
ζ_C	3.1(2)	3.05 (C _{21,22})
		3.01 (C _{23,25})
		3.09 (C _{24,26})
		3.12 (C _{27,31})
Spin Population (μ_B)		
Y 4d	0.01(1)	-0.01(1)
5s	0.07(2)	0.08(2)
O ₁ 2s	0.014	0.013
2p	0.11(1)	0.11 (1)
O ₂ 2s	0.027	0.025
2p	0.082(8)	0.09(1)
C ₂₁	0.25(1)	0.24(1)
C ₂₂	0.20 (1)	0.20(1)
C ₂₃	-0.02(1)	-0.02(1)
C ₂₄	0.15(1)	0.16(1)
C ₂₅	0.13(1)	0.12 (1)
C ₂₆	-0.01(1)	0.00 (1)
C ₂₇	0.01(1)	0.01 (1)
C ₃₁	0.010(9)	0.006(9)
total moment	1.04(4)	1.02(4)

of nitronyl–nitroxide (NN) radicals.^{49,50} The interaction of the semiquinonate with the yttrium atom induces mainly a lone pair dissymmetry as shown by a larger accumulation of electron density between oxygen and yttrium atoms, which is the signature of σ -donation.

Spin Density. The final refined spin populations are reported for the two types of radial models in Table 5. The sum of the populations for the different refinements is close to 1 μ_B , which confirms that the magnetization was near saturation during the experiment. The two models lead to close atomic spin populations and comparable agreement factors. The spin density, reconstructed from the final multipole refinement, is represented for the radial model A in Figure 3, in projection along the perpendicular to the radical ring and in projection along the C₂₁–C₂₂ direction. The corresponding maps for the radial model B are displayed in Figure 4. These maps are very similar, but the density appears to be more diffuse on Y in the model B.

Both maps give evidence of a spin delocalization (a few percent of the total moment) from the radical magnetic orbital toward the unoccupied orbitals of the Y³⁺ ion that lies in the rare earth site. The results reported in Table 5 show that the spin density delocalized on Y has mostly a 5s character. The projection maps in Figures 4b and 5b show that the spin density on the carbon atoms of the radical ring is mainly of π -type, while the oxygen 2p spin densities are tilted along the OC directions and mainly of σ character because of the existence of 2s and 2p_x significant contributions. The spin density appears to be highly delocalized on the C₂₁ and C₂₂ of C–O bonds and on the C₂₄ and C₂₅ of the radical ring. The populations of C₂₁ and C₂₂ are about double those of O₁ and O₂.

The most noticeable feature of the spin density distribution is the σ character observed on the oxygen atoms that could explain the relatively strong delocalization toward the diffuse 5s orbitals of the Y atom. This is in agreement with the oxygen lone pair polarization described above.

DFT Results. The ground electronic state of the Y(HBPz₃)₂(DTBSQ) is a ²A state with a HOMO–LUMO gap of about 2.4 eV. An isosurface representation ($|\psi| = 0.05$ au) of the SOMO is shown in Figure 5. The unpaired electron is mainly

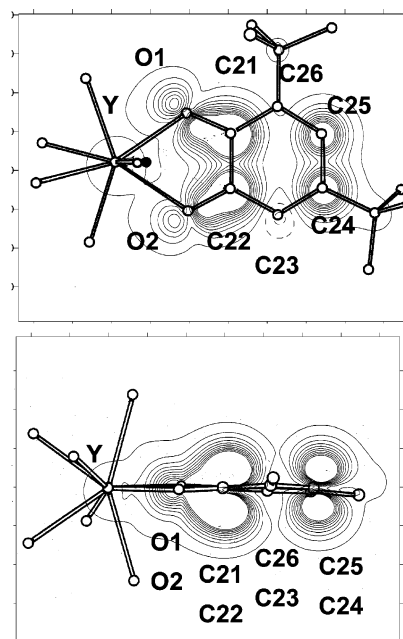


Figure 3. Projection of the induced spin density at 1.9 K under 9.5 T in Y(HBPz₃)₂(DTBSQ) obtained by multipole model A reconstruction: (a) along the perpendicular to the mean plane of the semiquinonate ring; (b) along the C₂₁–C₂₂ direction. Low levels only: $\pm 0.005 \mu_B/\text{\AA}^2$ with steps of $0.010 \mu_B/\text{\AA}^2$. Negative levels are dashed lines.

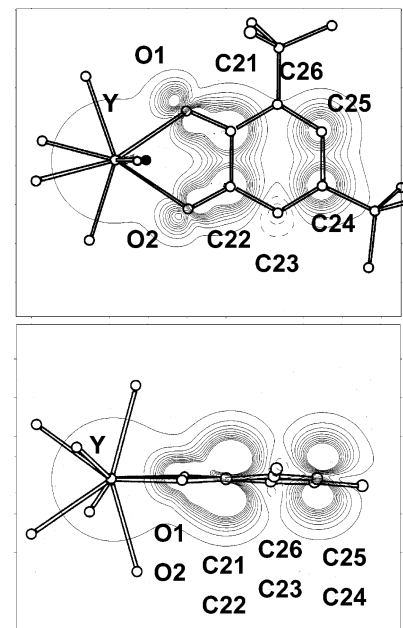


Figure 4. Same as Figure 3 for the multipole model B reconstruction.

delocalized onto the semiquinonate ligand, more precisely in the p-type atomic orbitals perpendicular to the aromatic ring.

The DFT charge populations, computed with the Mulliken population analysis⁵¹ reported in Table 6, cannot be directly compared to the experimental topological net atomic charges (Table 4). In Table 6 is reported another decomposition of the charge in the molecule, as suggested by Baerends,⁴⁹ namely, the Hirshfeld decomposition. The Hirshfeld charges are quite different from the Mulliken ones. They refer to a different decomposition of the space and cannot be compared to the experimental data, although they are also meaningful in order to analyze the bond. Surprisingly, as seen in Table 7, the Mulliken analysis yields a description which is close to the experiment. This agreement between topological charges and

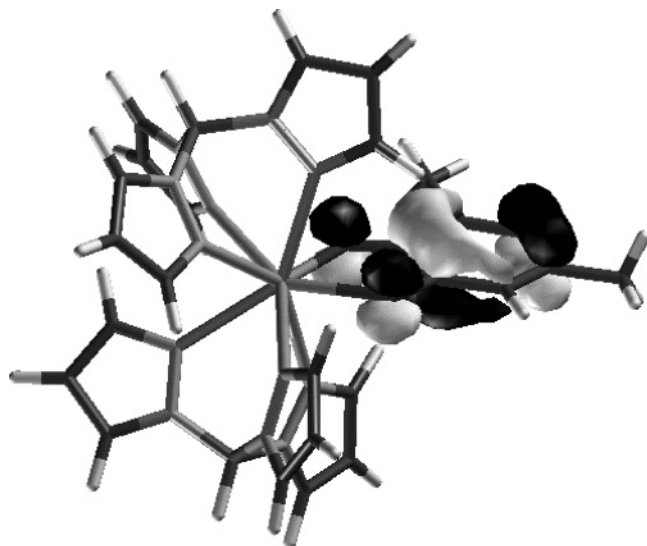


Figure 5. DFT magnetic orbital 107 α : highest occupied α orbital.

TABLE 6: Theoretical Atomic Charges (Mulliken and Hirshfeld) and Mulliken Spin Populations for Y(HBPz₃)₂(DTBSQ)

	Charge (e)		Mulliken Spin Population (μ_B)	
	Mulliken	Hirshfeld	LDA	GGA
Y	1.74	0.5880	0.0021	0.0037
O ₁	-0.80	-0.2185	0.2036	0.2040
O ₂	-0.80	-0.2166	0.1751	0.1761
C ₂₁	0.45	0.0790	0.1739	0.1842
C ₂₂	0.51	0.0851	0.1425	0.1499
C ₂₃	-0.36	-0.0760	0.0119	0.0010
C ₂₄	-0.05	0.0180	0.1125	0.1180
C ₂₅	-0.32	-0.0469	0.1499	0.1594
C ₂₆	-0.10	-0.0011	0.0123	-0.0039
C ₂₇	-0.82	-0.1467		
C ₃₁	-0.82	-0.1432		
N ₂	-0.50	-0.0924		
N ₄	-0.48	-0.1024		
N ₆	-0.50	-0.1018		
N ₁₂	-0.50	-0.0968		
N ₁₄	-0.48	-0.0979		
N ₁₆	-0.46	-0.0946		

Mulliken charges may appear surprising because the charge definition is not the same; it can, however, be understood because the overlap density in Figure 2 between Y and the O and N atoms is very small, which means that the contribution of the O and N atoms to the Y charge is negligible and vice versa; this is also confirmed by the expected bad agreement between most topological and Mulliken charges observed on the atoms of the radical linked together by covalent bonds (C23–C27 and C31; see Table 7 and Figure 1). The DFT total charge on the Y atom, computed with the Mulliken population analysis, is 1.74 e instead of 3 e for Y³⁺. The yttrium atomic valence populations correspond to a 4d^{0.88} 5s^{0.22} 5p^{0.16} configuration (instead of a 4d⁰ 5s⁰ 5p⁰ for Y³⁺), indicating that 1.26 e is transferred from the radical toward the Y³⁺ ion. As described above, the charge (+1.74 e) obtained on yttrium by DFT calculations is in agreement with the X-ray topological charge (+1.53 e), which is only half of the total formal charge (+3) for an Y³⁺ ion. This supports the idea that the electron transfer is approximately 1.5 e from the semiquinonate radical to the central ion. As far as the radical is concerned, the values given by DFT calculations for the oxygen atoms ($Q = -0.80$ e for both atoms) are close, once again, to the experimental net atomic charges ($Q = -1.08$ and -0.99 e for O₁ and O₂, respectively).

TABLE 7: Charge and Spin Populations for Y(HBPz₃)₂(DTBSQ)^a

	Charge (e)		Spin Population (μ_B)			
	exp	DFT	exp		DFT	
Y	1.53	1.74				
			4d/4p	0.08(2)	4d	0.004
				0.01(1)	4p	0.0038
			5s	0.07(2)	5s	0.0008
O ₁	-1.08	-0.80		0.122(10)		0.204
			2s	0.014(9)	2s	0.0037
			2p _x	0.096(65)	2p _x	0.0022
			2p _y	0.012(21)	2p _y	0.0026
			2p _z	0.000(1)	2p _z	0.1955
O ₂	-0.99	-0.80		0.109(8)		0.176
			2s	0.027(10)	2s	0.0029
			2p _x	0.079(30)	2p _x	0.0021
			2p _y	0.010(47)	2p _y	0.0022
			2p _z	0.003(1)	2p _z	0.1688
C ₂₁	0.57	0.45		0.25(1)		0.184
C ₂₂	0.44	0.51		0.20(1)		0.150
C ₂₃	0.01	-0.36		-0.02(1)		0.001
C ₂₄	0.29	-0.05		0.15(1)		0.118
C ₂₅	-0.25	-0.32		0.13 (1)		0.159
C ₂₆	0.42	-0.10		-0.01 (1)		-0.004
C ₂₇	0.19	-0.82		0.01 (1)		
C ₃₁	0.21	-0.82		0.01 (1)		
N ₂	-0.58	-0.50				
N ₄	-0.56	-0.48				
N ₆	-0.53	-0.50				
N ₁₂	-0.51	-0.50				
N ₁₄	-0.59	-0.48				
N ₁₆	-0.57	-0.46				

^a Experimental: topological atomic charges and spin populations from model A refinement. Theoretical DFT: Mulliken charge and spin populations (ZORA-GGA).

Also, the population of $-0.50(1)$ e given by DFT calculations on the nitrogen atoms coordinating the central yttrium is close to the average $-0.56(3)$ e experimental charge.

The distribution of the electronic spin over the molecule can be conveniently described by the Mulliken spin population analysis that partitions the spin density, $\rho^{\alpha}(r) = \rho^{\alpha}(r) - \rho^{\beta}(r)$, over the atoms of the paramagnetic molecule. The computed spin populations, which are affected by all the deficiencies of the Mulliken population analysis, can be directly compared to the populations obtained from the polarized neutron diffraction experiment (Tables 6 and 5, respectively). In the same table, we also compare the spin populations computed with LDA and GGA. The two computational approaches give comparable values when spin populations are larger than $0.1 \mu_B$ but differ for smaller populations. It must be remembered, however, that any partition scheme suffers from some approximation, and small numbers should be meaningful only for comparison between series of complexes. Also, the spin densities coming from neutron diffraction experiments are partitioned in atomic spin populations by fitting the magnetic structure factors of the measured reflections with Slater atomic orbitals. To reduce the number of parameters, the quantity of functions included in the fit is smaller than that in the atomic minimal basis set. Consequently, the individual atomic orbital contributions cannot be directly compared to the atomic orbital contributions coming from a calculation.

It appears from Table 7 that an overall agreement with the experimental spin densities is achieved with the GGA results. In particular, 99% of the spin density is computed onto the semiquinonate radical with a small contribution on the Y atom. These results agree nicely with the experimental findings even if the computed spin density on Y is definitely smaller than the

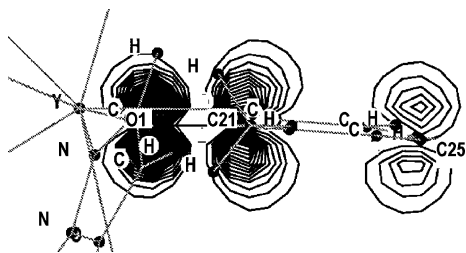


Figure 6. Section of the theoretical DFT spin density in $e \text{ \AA}^{-3}$ in the yz plane (z being the direction perpendicular to the semiquinonate plane and y being along the O_1-C_{21} direction). Contours of $0.002 e \text{ \AA}^{-3}$.

experimental one (10 times smaller). Moreover, the delocalization of the spin on the carbon atoms of the radical ring is underestimated with respect to the experimental distribution. The spin populations on C_{21} and O_1 are larger than those on C_{22} and O_2 , as observed. It is noteworthy that the spin populations experimentally obtained on the oxygen atoms are lower than those for the $C_{21}-C_{22}$ carbon atoms, while theoretically, we obtain almost the same populations. This distribution is also different from those observed on nitronyl-nitroxide radicals for which the unpaired electron is shared equally by oxygen and nitrogen atoms.

The DFT calculations predict that the unpaired spin is located in a π -type orbital delocalized on the oxygen atoms and the carbon atoms of the ring. In particular, the DFT spin populations of both oxygen atoms correspond to an occupation of 98% of the $2p_z$ orbital plane, as indicated by the orbital populations given in Table 7 (z being the direction perpendicular to the semiquinonate plane). This is illustrated in Figure 6 by the section of the theoretical spin density in the plane perpendicular to the semiquinonate plane along the O_1-C_{21} direction. This is not in agreement with the experimental spin density map, which shows that the shape of the spin density on both oxygen atoms is of σ -type, elongated along the $O-C$ bonds. The $2s$ and $2p$ orbital coefficients obtained from the neutron data refinement are reported in Table 7. For both oxygen atoms, the $2p_x$ and $2s$ coefficients are significantly larger than the error bar (x is the $O-C$ bond direction). Where the Y atom is concerned, the theoretical spin distribution predicts that the Y spin population is mainly of $4d$ -type, as shown by the orbital populations in Table 7, contrary to the experimental result which indicates a more pronounced $5s$ character.

Conclusions

The study of the electron density highlights some characteristics of this yttrium-semiquinonate complex. First, we observe that contacts between yttrium and oxygen atoms appear to be stronger than those with nitrogen atoms. This fact is confirmed by the net atomic charges, which show the expected result on the two HBPZ₃ but indicate an electron transfer of approximately 1.5 e between the central yttrium ion and the semiquinonate radical. Interactions with the central Y atom slightly polarize the oxygen lone pair density which indicates σ -donation in the Y-O bonding.

The experimental spin density provides evidence of a significant spin delocalization from the radical onto the rare earth site showing that, in principle, sizable magnetic coupling can be achieved with a magnetic rare earth ion. This could be due to the σ nature of the oxygen spin distribution.

The DFT calculations are in good agreement with the experimental charge distribution but only in qualitative agreement with the spin distribution. The theoretical spin population on the Y site is 1 order of magnitude smaller than the

experimental population. The value of the spin delocalization from the oxygen atom toward the carbon ring is underestimated. Finally, the tilt of the oxygen spin density distributions is not reproduced by the DFT calculations.

The observed delocalization from the radical π orbital toward the unoccupied $4d$ or $5s$ orbitals of the Y^{3+} ion, which lies in the rare earth site, supports the interpretation of the nature of the magnetic interaction between a rare earth ion, Gd^{3+} , and a radical as resulting from the competition between two terms: (i) an antiferromagnetic contribution due to the direct overlap between the rare earth magnetic orbitals and the magnetic orbital of the radical, which dominates in the case of the Gd-semiquinonate complex; and (ii) a ferromagnetic contribution due to the delocalization from the radical magnetic orbital toward the unoccupied $5d$ or $6s$ orbitals of Gd^{3+} resulting in a polarization of the $4f$ electrons in a parallel way to the unpaired electron of the radical.

Attempts are currently being made to analyze the analogous data on the gadolinium derivative.

Acknowledgment. Dante Gatteschi and his collaborators thank MOLNANOMAG HPRN-CT-1999-00012 and Italian MIUR. Yves Pontillon thanks 3MD ERB FMRX CT98 0181. Nicolas Claiser thanks the Ministère de la Recherche for a Ph.D. fellowship.

Supporting Information Available: X-ray data collection: evolution of the agreement factors by resolution envelopes in \AA^{-1} and evolution of the mean observed intensity $\langle I \rangle$ and mean ratio $\langle I/\sigma(I) \rangle$ by resolution envelopes. Magnetic data: the product of magnetic susceptibility and temperature, χT , and the magnetization as functions of temperature. This material is available free of charge via the Internet at <http://pubs.acs.org>.

References and Notes

- Benelli, C.; Gatteschi, D. *Chem. Rev.* **2002**, *102*, 2369.
- Benelli, C.; Caneschi, A.; Fabretti, A. C.; Gatteschi, D.; Pardi, L. *Inorg. Chem.* **1990**, *29*, 4153.
- Caneschi, A.; Dei, A.; Gatteschi, D.; Sorace, L.; Vostrikova, K. *Angew. Chem., Int. Ed.* **2000**, *39*, 1750.
- Benelli, C.; Caneschi, A.; Gatteschi, D.; Pardi, L.; Rey, P. *Inorg. Chem.* **1989**, *28*, 3230.
- Guillou, O.; Bergerat, P.; Kahn, O.; Bakalbassis, E.; Boubeker, K.; Batail, P.; Guillot, M. *Inorg. Chem.* **1992**, *31*, 110.
- Champion, G.; Lalioi, N.; Tangoulis, V.; Arrio, M.-A.; Saintavrit, P.; Villain, F.; Caneschi, A.; Gatteschi, D.; Giorgetti, C.; Baudelet, F.; Verdager, M.; Cartier dit Moulin, C. *J. Am. Chem. Soc.* **2003**, *125*, 8371.
- (a) Figgis, B. N.; Kucharski, E. S.; Williams, G. A. *J. Chem. Soc., Dalton Trans.* **1980**, 1515. (b) Figgis, B. N.; Williams, G. A.; Forsyth, J. B.; Mason, R. *J. Chem. Soc., Dalton Trans.* **1981**, 1837.
- (a) Figgis, B. N.; Reynolds, P. A.; Williams, G. A. *J. Chem. Soc., Dalton Trans.* **1980**, 2339. (b) Figgis, B. N.; Reynolds, P. A.; White, A. H. *J. Chem. Soc., Dalton Trans.* **1987**, 1737.
- (a) Figgis, B. N.; Reynolds, P. A.; Mason, R. *J. Am. Chem. Soc.* **1983**, *105*, 434. (b) Figgis, B. N.; Reynolds, P. A.; Mason, R. *J. Am. Chem. Soc.* **1983**, *105*, 440.
- (a) Figgis, B. N.; Reynolds, P. A.; Mason, R. *Inorg. Chem.* **1984**, *23*, 1149. (b) Figgis, B. N.; Reynolds, P. A.; White, A. H. *Inorg. Chem.* **1985**, *24*, 3762.
- (a) Figgis, B. N.; Kucharski, E. S.; Reynolds, P. A. *Acta Crystallogr. B* **1990**, *46*, 577. (b) Delfs, C. D.; Figgis, B. N.; Forsyth, J. B.; Kucharski, E. S.; Reynolds, P. A.; Vrtis, M. *Proc. R. Soc. London A* **1992**, *436*, 417.
- (a) Reynolds, P. A.; Figgis, B. N. *Inorg. Chem.* **1985**, *24*, 1864. (b) Figgis, B. N.; Kucharski, E. S.; Vrtis, M. *J. Am. Chem. Soc.* **1993**, *115*, 176.
- Pontillon, Y.; Bencini, A.; Caneschi, A.; Dei, A.; Gatteschi, D.; Gillon, B.; Sangregorio, C.; Stride, J.; Totti, F. *Angew. Chem., Int. Ed.* **2000**, *39*, 1786.
- Trofimenko, S. *Inorg. Synth.* **1970**, *12*, 99.
- Mass, M. J.; Jones, C. J. *J. Chem. Soc., Dalton Trans.* **1990**, 581.
- Otwinowski, Z.; Minor, W. *Methods in Enzymology*. In *Macromolecular Crystallography, Part A* (307); Carter, C. W., Jr., Sweet, R. M., Eds.; New York Academic Press: New York, 1996; Vol. 276.

- (17) DeTitta, G. T. *J. Appl. Cryst.* **1985**, *18*, 75.
(18) Blessing, R. H. *J. Appl. Cryst.* **1989**, *22*, 396.
(19) French, S.; Wilson, K. *Acta Crystallogr.* **1978**, *A34*, 517.
(20) Lehmann, M. S.; Larsen, F. K. *Acta Crystallogr.* **1974**, *A30*, 580.
(21) Schweizer, J.; Gillon, B. In *Magnetic Properties of Organic Radicals*; Lahti, P. M., Ed.; Marcel Dekker: New York, 1999; p 449.
(22) Papoular, R. J.; Gillon, B. *Europhys. Lett.* **1990**, *13*, 429.
(23) Brown, P. J.; Capiomont, A.; Gillon, B.; Schweizer, J. *J. Magn. Mater.* **1979**, *14*, 289.
(24) Te Velde, G.; Bickelhaupt, F. M.; Baerends, E. J.; Fonseca Guerra, C.; Van Gisbergen, S. J. A.; Snijders, J. G.; Ziegler, T. *J. Comput. Chem.* **2001**, *22*, 931.
(25) Slater, C. *Quantum Theory of Molecules and Solids*; McGraw-Hill: New York, 1974; Vol. 4.
(26) Vosko, S. J.; Wilk, L.; Nusair, M. *Can. J. Phys.* **1980**, *58*, 1200.
(27) (a) Perdew, J. P. In *Electronic Structure of Solids '91*; Ziesche, P., Eschrig, H., Eds.; Akademie Verlag: Berlin, 1991; p 11. (b) Perdew, J. P.; Chevary, J. A.; Vosko, S. H.; Jackson, K. A.; Pederson, M. R.; Singh, D. J.; Fiolhais, C. *Phys. Rev. B* **1992**, *46*, 6671; **1993**, *48*, 4978(E).
(28) (a) van Lenthe, E.; Ehlers, A. E.; Baerends, E. J. *J. Chem. Phys.* **1999**, *110*, 8943. (b) van Lenthe, E.; Baerends, E. J.; Snijders, J. G. *J. Chem. Phys.* **1993**, *99*, 4597. (c) van Lenthe, E.; Baerends, E. J.; Snijders, J. G. *J. Chem. Phys.* **1994**, *101*, 9783. (d) van Lenthe, E.; Snijders, J. G.; Baerends, E. J. *J. Chem. Phys.* **1996**, *105*, 6505. (e) van Lenthe, E. et al. *Int. J. Quantum Chem.* **1996**, *57*, 281.
(29) Dei, A.; Gatteschi, D.; Pécaut, J.; Poussereau, S.; Sorace, L.; Vostrikova, K. *C. R. Acad. Sci. Paris* **2001**, *4*, 135–141.
(30) Sheldrick, G. M. *Acta Crystallogr.* **1990**, *A46*, 467.
(31) Sheldrick, G. M. *SHELXL97*; University of Göttingen: Göttingen, Germany, 1997.
(32) Hansen, N. K.; Coppens, P. *Acta Crystallogr.* **1978**, *A34*, 909.
(33) Roetti, C.; Clementi, E. *J. Chem. Phys.* **1974**, *60*, 4725.
(34) Stewart, R. F.; Davidson, E. R.; Simpson, W. T. *J. Chem. Phys.* **1965**, *43*, 175.
(35) Cromer, D. T. *International Tables for X-ray Crystallography*, 148, Ibers, J. A., Hamilton, W. E., Eds.; Kynoch Press: Birmingham, 1974.
(36) Guillot, B.; Viry, L.; Guillot, R.; Lecomte, C.; Jelsch, C. *J. Appl. Crystallogr.* **2001**, *34*, 214.
(37) Bader, R. F. W. *Atoms in Molecules: A Quantum Theory*. The International Series Monographs in Chemistry; Oxford Clarendon Press, 1990.
(38) Souhassou, M.; Blessing, R. H. *J. Appl. Crystallogr.* **1999**, *32*, 210.
(39) Clementi, E.; Roetti, C. *At. Data Nucl. Data Tables* **1974**, *14*, 177.
(40) Boucherle, J. X.; Gillon, B.; Maruani, J.; Schweizer, J. *Mol. Phys.* **1987**, *60*, 1121.
(41) Schweizer, J.; Ressouche, E. *MagnetoScience: From Molecules to Materials*; Miller, J., Drillon, M., Eds.; Wiley: New York, 2001; p 325.
(42) Buchanan, R. M.; Pierpont, C. G. *J. Am. Chem. Soc.* **1980**, *102*, 4951–4957.
(43) Ruf, M.; Noll, B. C.; Groner, M. D.; Yee, G. T.; Pierpont, C. G. *Inorg. Chem.* **1997**, *36*, 4860–4865.
(44) Jung, O.-S.; Pierpont, C. G. *Inorg. Chem.* **1994**, *33*, 2227–2235.
(45) Lange, C. W.; Pierpont, C. G. *Inorg. Chim. Acta* **1997**, *41*, 219–224.
(46) Jung, O.-S.; Jo, D. H.; Lee, Y.-A.; Sohn, Y. S.; Pierpont, C. G. *Inorg. Chem.* **1998**, *37*, 5875–5880.
(47) Caneschi, A.; Dei, A.; Gatteschi, D.; Tangoulis, V. *Inorg. Chem.* **2002**, *41*, 3508–3512.
(48) Claiser, N.; Souhassou, M.; Lecomte, C. Problems in Experimental Charge Density Modelling of Rare Earth Atom Complexes: the Case of Gadolinium. *J. Phys. Chem. Solids* **2004**, *65*, 1927.
(49) Pillet, S.; Souhassou, M.; Pontillon, Y.; Caneschi, A.; Gatteschi, D.; Lecomte, C. *New. J. Chem.* **2001**, *25*, 131.
(50) Claiser, N.; Souhassou, M.; Lecomte, C.; Pontillon, Y.; Romero, F. M.; Ziessel, R. *J. Phys. Chem. B* **2002**, *106*, 12896.
(51) Mulliken, R. S. *J. Chem. Phys.* **1962**, *36*, 342.
(52) Guerra, C. F.; Handgraaf, J. W.; Baerends, E. J.; Bickelhaupt, F. M. *J. Comput. Chem.* **2004**, *25*, 189.